Plasmon-Induced Hot Carriers in Metallic Nanoparticles

Alejandro Manjavacas,* Jun G. Liu, Vikram Kulkarni, and Peter Nordlander*

Department of Physics and Astronomy and Laboratory for Nanophotonics, Rice University, Houston, Texas 77005, United States

ABSTRACT Plasmon-induced hot carrier formation is attracting an increasing research interest due to its potential for applications in photocatalysis, photodetection and solar energy harvesting. However, despite very significant experimental effort, a comprehensive theoretical description of the hot carrier generation process is still missing. In this work we develop a theoretical model for the plasmon-induced hot carrier process and apply it to spherical silver nanoparticles and nanoshells. In this model, the conduction electrons of the metal are described as free particles in a finite spherical potential well, and the plasmon-induced hot carrier production is calculated using Fermi's golden rule. We show that the inclusion of many-body interactions has only a minor influence on the results. Using the model we calculate the rate of hot carrier generation, finding that it closely follows the spectral profile of the plasmon. Our analysis reveals that particle size and hot carrier lifetime play a central role in determining both the production rate and the energy distribution of the hot carriers. Specifically, larger nanoparticle sizes and shorter lifetimes result in higher carrier production rates but smaller energies, and vice versa. We characterize the efficiency of the hot carrier generation process by introducing a figure of merit that measures the number of high energy carriers generated per plasmon. Furthermore, we analyze the spatial distribution and directionality of these excitations. The results presented here contribute to the basic understanding of plasmon-induced hot carrier generation and provide insight for optimization of the process.

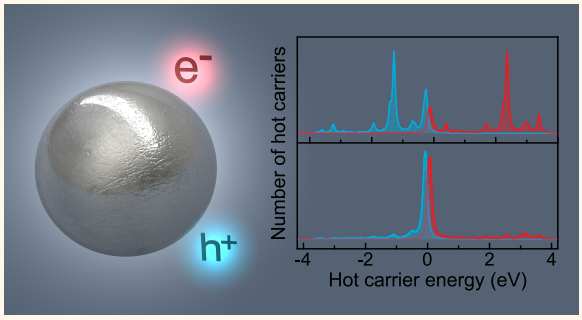

KEYWORDS: hot electrons · hot carriers · plasmons · plasmon decay · nonradiative decay · nanoparticle · nanophotonics

The collective excitations of the conduction electrons of metallic nanostructures, known as surface plasmons, have become a key element in nanophotonics due to their exceptional ability to capture far-field radiation and concentrate it into subwavelength volumes well below the diffraction limit,[1,2] thus producing strong near-fields that result in extreme field enhancements.[3] These extraordinary properties have fueled the development of novel applications in different areas such as ultrasensitive biosensing,[4,5] photothermal cancer therapy,[6,7] drug delivery,[8,9] or improved photovoltaic devices.[10,11]

Surface plasmons have finite lifetimes after which they decay either radiatively by emitting a photon, or nonradiatively by generating electron–hole pairs. The radiative decay channel has been extensively utilized in the past decade to optimize, for instance, efficient nanoantennas capable of enhancing and directing the radiation of single emitters.[12–14] More recently, a considerable research effort has been directed to exploit the hot carriers generated through the nonradiative decay channel in applications.[15,16] These hot carriers are capable of inducing chemical reactions in molecules in the vicinity of the surfaces of plasmonic nanostructures, which would otherwise be energetically very demanding.[17] Different experiments involving water splitting,[18–23] hydrogen dissociation,[24,25] and the generation of hydrogen from ethanol[26,27] have already been demonstrated, thus fueling the growth of this new field of plasmon-enabled photochemistry.[28,29] Plasmon-induced hot carriers also provide an efficient mechanism to convert light into electric current[30–32] that can be used for developing alternative solar-energy harvesting devices,[33,34] or to design efficient photodetectors with spectral responses circumventing band gap limitations.[35–37] These excitations can also be injected in other materials, such as graphene, thus enabling plasmon-induced phase transitions and doping mechanisms.[38–40]

Although direct excitation of hot carriers on metal surfaces is possible and has since long been exploited in the field of surface femtochemistry,[41] the utilization of surface

* Address correspondence to alejandro.manjavacas@rice.edu, nordland@rice.edu.

Received for review May 5, 2014 and accepted June 24, 2014.

Published online June 24, 2014
10.1021/nn502445f

plasmon decay to increase the efficiency of the hot carrier generation process is relatively novel. The basis for this dramatic enhancement is the large plasmon-induced field enhancement and the dramatically enhanced light harvesting capability of the collective plasmon excitations.[1−3] However, in order to exploit these advantages we need to understand the physical processes behind plasmon-induced hot carrier generation. This requires the development of an appropriate theoretical framework, which despite the significant experimental effort, is still not complete.[42−46]

In this article we develop a simple model to describe the generation of plasmon-induced hot carriers in silver nanoparticles and nanoshells. The model is based on describing the conduction electrons of the metal as free particles and then analyzing the plasmon-induced dynamics using Fermi's golden rule. Interestingly, we find that the inclusion of many-body interactions only has a minor impact in the results. Using this model, we calculate the number of hot carriers generated per unit time as a function of the illumination frequency, obtaining a spectral profile that closely follows the plasmonic spectrum. Furthermore, we find that the number and the energy distribution of these excitations depend strongly on the size of the nanoparticle and on the carrier lifetime. In order to quantify the efficiency of the process, we introduce a figure of merit that measures the number of high energy carriers generated per plasmon. We complete our analysis by investigating the spatial distribution and the directionality of these excitations.

RESULTS AND DISCUSSION

Description of the Model. The system under study is depicted in Figure 1(a). We consider a silver nanoparticle with a diameter D ranging from 5 to 25 nm. We model the conduction electrons of this system as free particles in a finite spherical potential well with a depth V_0, which is chosen to ensure an appropriate workfunction (4.5 eV) for silver. Using this potential we solve the corresponding Schrödinger equation (see Methods) to obtain the electron energies ε_i and wave functions $\Psi_i(\mathbf{r})$. In our model we only consider the conduction electrons of the metal, which is a very good approximation for silver since in this material the energy difference between the d-band electrons and the Fermi level is larger than the plasmon energy. However, in other materials such as gold, electrons from the d-band can contribute significantly to the hot carrier generation process.[16] Furthermore, we assume that the particle is illuminated with a linearly polarized electric field oscillating at frequency ω (see Figure 1(a)), which corresponds to a wavelength $\lambda = 2\pi c/\omega$. Since the relevant wavelengths are much larger than the particle sizes studied here (*i.e.*, $\lambda \gg D$), we can neglect phase retardation effects and work in the quasi-static regime. Within this limit, it is sufficient to consider the electric potential associated with the field, which in turn can be assumed to be uniform over the particle size. By doing so, the potential corresponding to the external field can be written as $V_{ext}(\mathbf{r},\omega) = -E_0 r \cos\theta$, where E_0 the field amplitude, r the radial distance,

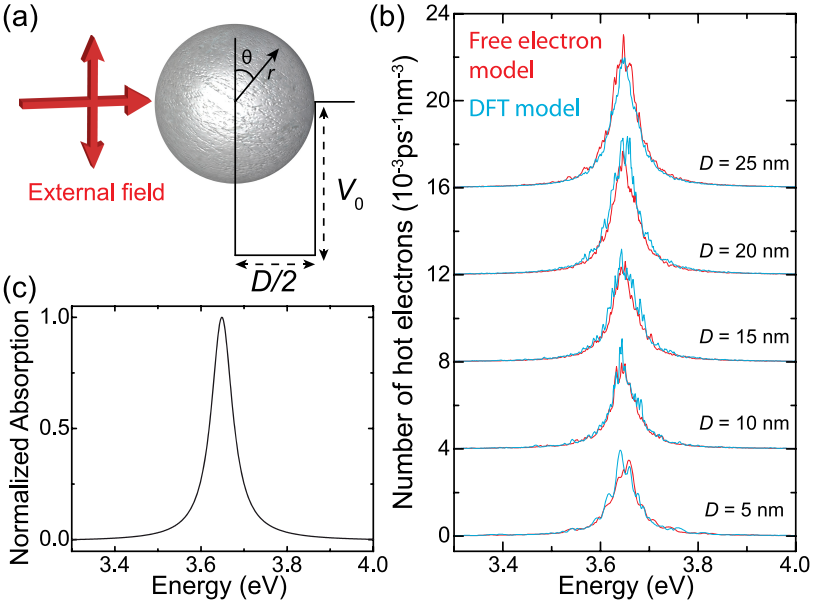

Figure 1. Plasmon-induced hot electron production in a silver nanoparticle. (a) Schematic representation of the system under study. We consider a silver nanoparticle of diameter D. We model the conduction electrons of this structure as free particles in a finite spherical potential well of depth V_0 and radius equal to $D/2$. (b) Number of hot electrons generated per unit of time and volume as a function of the frequency of the external illumination. We plot this magnitude for different nanoparticle diameters ranging from 5 to 25 nm using the energies and wave functions obtained with a free electron model (red lines) and with a density functional theory (DFT) approach (blue lines) (see main text for more details). In all cases the hot carrier lifetime is assumed $\tau = 0.5$ ps and the intensity of the external illumination is 1 mW μm^{-2}. All curves offset for clarity. (c) Normalized absorption for the silver nanoparticle calculated in the quasi-static limit.

and θ the polar angle. The external illumination results in the excitation of a plasmon in the nanoparticle whose induced electric potential is $V_p(\mathbf{r},\omega) = (\varepsilon - 1)/(\varepsilon + 2)E_0 r\cos\theta$ inside the metal, and $V_p(\mathbf{r},\omega) = (\varepsilon - 1)/(\varepsilon + 2)D^3/(8r^2)E_0\cos\theta$ outside. Here, ε is the dielectric function of silver, which we describe using the Drude model[47] $\varepsilon = \varepsilon_b - \omega_{pl}^2/\omega/(\omega + i\gamma)$, with a background dielectric function $\varepsilon_b = 4.18$, a plasma frequency $\omega_{pl} = 9.07$ eV, and a plasmon damping of $\gamma = 60$ meV. These values are chosen to accurately reproduce the experimental permittivity in the frequency region of interest ($\approx$ 3−4 eV). In our semiclassical model, we treat the plasmon excitation as a classical field. Although plasmon modes strictly speaking are quantum mechanical bosonic excitations with an energy dispersion given by $\hbar\omega_p(n + (1/2))$, where ω_p is the plasmon frequency, the cross sections for excitations of bright plasmon modes are typically so large that the plasmon is excited to a sufficiently large quantum number n that the plasmon field can be treated classically.

Hot carriers are generated by the action of the external and the plasmon-induced electric potentials, which interact with the conduction electrons of silver, inducing transitions from an initial state Ψ_i, located below the Fermi level, to a final state Ψ_f above it. During this transition, the plasmon occupation number in the particle is reduced by one unit (*i.e.*, $n \rightarrow n - 1$). This process creates two excited carriers: a hole in state Ψ_i, and an electron in the state Ψ_f. In a situation where the energy difference between the excited electron or hole and the Fermi level has a larger magnitude than the energies of the relevant thermal excitations, these carriers are referred to as hot electrons or holes or both.

The Hamiltonian that describes this process can be written as

$$\mathcal{H} = \int d\mathbf{r}[V(\mathbf{r},\omega) + V^*(\mathbf{r},\omega)]\sum_{i,f}\rho_{fi}(\mathbf{r})b_f^\dagger b_i$$

Here, $V(\mathbf{r},\omega)$ is the total potential (*i.e.*, $V_{ext} + V_p$), $\rho_{fi}(\mathbf{r}) = e\Psi_f^*(\mathbf{r})\Psi_i(\mathbf{r})$ where e is the elementary charge, and $b_i^\dagger(b_i)$ is the operator that creates an electron (hole) in state Ψ_i. Using this Hamiltonian, the probability per unit time of exciting a hot electron in state f can be calculated using Fermi's golden rule[48]

$$\Gamma_e(\varepsilon_f,\omega) = \frac{4}{\tau}\sum_i \mathcal{F}(\varepsilon_i)[1 - \mathcal{F}(\varepsilon_f)]\left\{\frac{|M_{fi}(\omega)|^2}{(\hbar\omega - \varepsilon_f + \varepsilon_i)^2 + \hbar^2\tau^{-2}} + \frac{|M_{if}^*(\omega)|^2}{(\hbar\omega + \varepsilon_f - \varepsilon_i)^2 + \hbar^2\tau^{-2}}\right\} \quad (1)$$

where $\mathcal{F}$ is the Fermi−Dirac distribution function, in which for simplicity we assume zero temperature, $M_{fi} = \int d\mathbf{r}V(\mathbf{r},\omega)\rho_{fi}(\mathbf{r})$ is the transition matrix element, and we have included a factor of 2 to account for the spin. The probability per unit time of exciting a hot hole in state f (*i.e.*, $\Gamma_h(\varepsilon_f,\omega)$) can be directly obtained by interchanging the subscripts i and f in eq 1 after the summation symbol.

It is well-known[49−52] that after being generated, the hot carriers thermalize through electron−electron and electron-surface scattering, and eventually cool down *via* electron−phonon scattering, releasing their energy to the lattice and heating up the particle. We effectively incorporate all these decay mechanisms through the introduction of a finite lifetime τ for the hot carriers. This is done here by replacing the Dirac delta function of Fermi's golden rule with a Lorentzian function of width τ^{-1}. This finite lifetime is needed to obtain a realistic description of the electronic structure and density of states and plays a crucial role in the hot carrier generation process that will be discussed in the following sections. We note that the physics underlying this broadening relates to processes that happen after the initial formation of hot carriers and that τ in principle could be calculated by directly including electron−electron and electron−phonon interactions. It is important to remark that this excited carrier lifetime τ is physically distinct from the plasmon damping γ, which determines the lifetime of the plasmon excitation.

The model presented here involves three main approximations: (i) the hot carrier lifetime τ effectively accounts for all possible hot carrier decay mechanisms; (ii) the electrons are assumed to remain in their ground state even when a plasmon is excited; and (iii) the plasmon is assumed to lose only a single plasmon quantum during each hot carrier generation process. These assumptions are realistic given the short lifetime ($\approx$ 10 fs) of the plasmon excitation, the large cross section for plasmon excitation that results in plasmons being excited to high quantum numbers n, and the sequential nature of nonradiative plasmon decay.

The small size of the particles under study makes the radiative decay channel negligible. This means that all energy absorbed by the particle from the external illumination must be dissipated into hot carriers. The power absorbed by the nanoparticle, $P_{abs} = (\omega/4)D^3 Im\{(\varepsilon - 1)/(\varepsilon + 2)\}E_0^2$, is controlled by the parameters of the Drude model and the geometry of the nanoparticle. For this reason, conservation of energy must be imposed in our model by rescaling the generation rate (*i.e.*, eq 1) with an appropriate factor calculated as the ratio between the power absorbed and the power dissipated in the hot carrier generation.

We note that with the incorporation of an effective lifetime τ of the excited carriers, the model developed here allows us to compute the steady state hot carrier distribution during continuous light illumination. The results presented in this paper thus provide a quantitative description for the case of pulsed illumination as long as the duration of the pulse is larger than τ. More importantly, our model provides a basis for the modeling of the time dependent relaxation of excited carriers. By reducing the effective lifetime τ to its natural line width, eq 1 would describe the instantaneous carrier generation from plasmon decay in the system.

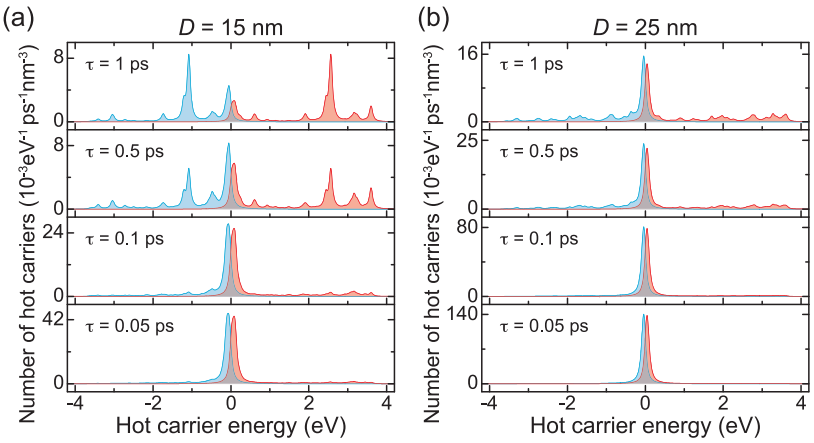

Figure 2. Hot carrier distribution. We plot the number of hot electrons (red lines) and hot holes (blue lines) generated per unit of time and volume as a function of their energy. We consider four different hot carrier lifetimes τ ranging from 0.05 to 1 ps, and two nanoparticle diameters: $D = 15$ nm (a), and $D = 25$ nm (b). The frequency of the external illumination is fixed to 3.65 eV, which corresponds to the plasmon frequency and therefore to the maximum absorption (see Figure 1(c)). Zero energy refers to the Fermi level.

The dynamics of the excited carriers can then be followed by coupling the various excitations in the system. In such an approach, it will be possible to assess the relative importance and time scales of electron-impurity, electron–electron, and electron–phonon interactions.

Size and Lifetime Dependence. Figure 1(b) shows the total number of hot electrons generated per unit of time and volume as a function of the frequency of the external illumination. We calculate the hot electron production rates for nanoparticles of different diameters using eq 1 by summing over all possible final states. In all cases, we assume an illumination intensity of 1 mW μm^{-2} and a hot carrier lifetime of $\tau = 0.5$ ps. The results plotted with red lines have been obtained using the free electron wave functions and energies, as explained in the previous section. We compare them with equivalent calculations (blue lines) in which we use wave functions and energies that incorporate many-body effects as included within the density functional theory (DFT) methodology (see Methods). From this comparison we conclude that such exchange-correlation effects have only a minor impact on the hot carrier generation and therefore can be ignored at the present level of approximation. We expect to find even better agreement in materials with larger workfunctions and smaller plasmonic energies, for which the relevant electronic states lay deeper in the potential well. Interestingly, the number of hot electrons generated closely follows the absorption spectrum with some oscillations originated from the discreteness of the electronic levels of the nanoparticles (*cf.* Figure 1(b,c)). Since the optical absorption in these systems is totally controlled by the supported plasmons, the peaking of the hot electron production rate at the plasmon resonance confirms the dominant role played by these excitations in the generation of hot carriers. Clearly, the excitation of plasmons, with their strong associated near-fields and dramatically enhanced absorption cross section, enhances the hot carrier generation by several orders of magnitude compared to direct excitation of hot electrons by the external field.

Keeping in mind the potential applications of plasmon-induced hot carriers, it is important to investigate not only the total number of carriers generated at a certain frequency, but also their energy distribution. This is done in Figure 2, where we plot the energy of the hot carriers generated by silver nanoparticles with diameters of 15 nm (panel (a)) and 25 nm (panel (b)). We perform this calculation for the plasmon frequency ($\hbar\omega_p$ = 3.65 eV) at which the absorption reaches its maximum (see Figure 1(c)) using four different hot carrier lifetimes τ. So far (*e.g.*, in Figure 1(b)), we have considered a hot carrier lifetime of $\tau = 0.5$ ps, to be consistent with other theoretical studies.[44−46] However, we note that experimental measurements of excited carrier lifetimes have shown that hot carrier lifetimes can range from 0.05 to 1 ps.[49−52] Interestingly, the actual value of the lifetime τ turns out to be of crucial importance since, as shown in Figure 2, the energy distribution of the hot carriers change dramatically as this magnitude is varied within that range. In particular, long lifetimes result in the generation of carriers with large energies, which can be a significant fraction of the excitation frequency ($\hbar\omega$ = 3.65 eV). On the contrary, smaller values favor the generation of carriers with close to thermal energies (*i.e.*, near the Fermi level). A similar behavior is observed when the size of the nanoparticle is varied, keeping the lifetime fixed. In this case, larger diameters produce less energetic carriers and vice versa (*cf.* panels (a) and (b) of Figure 2). The origin of this behavior can be traced to the density of electronic states of these systems. Specifically, systems with a finite number of electrons have a finite number of energy levels and therefore, a discrete density of states. However, a finite lifetime introduces a level broadening inversely proportional

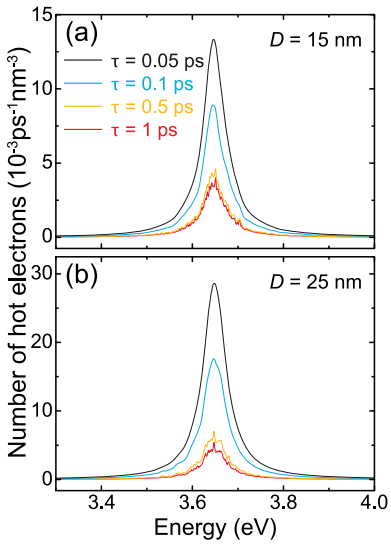

Figure 3. Effect of the hot carrier lifetime τ. Number of hot electrons generated per unit of time and volume as a function of the frequency of the external illumination for different hot carrier lifetimes τ ranging from 0.05 to 1 ps. Panel (a) shows the results for a nanoparticle diameter of D = 15 nm and panel (b) for D = 25 nm.

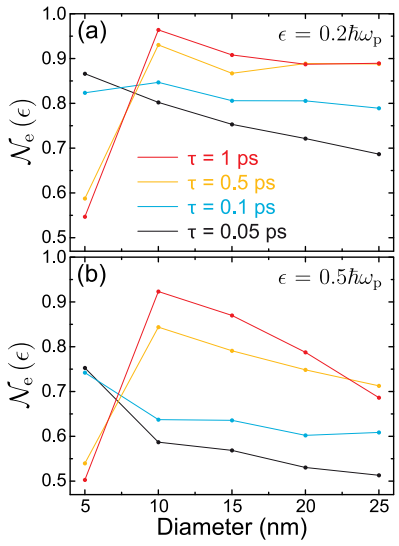

Figure 4. Efficiency (FoM) of the plasmon-induced hot carrier generation. (a) Number of hot electrons generated per each plasmon excited in the system that have an energy larger than $\varepsilon = 0.2\hbar\omega_p$. (b) Same as panel (a) with $\varepsilon = 0.5\hbar\omega_p$. In both cases we plot the FoM as a function of the nanoparticle diameter for four different hot carrier lifetimes τ (see legend).

to its value. As a result of this, the density of states is turned into a continuous distribution that becomes more homogeneous as the lifetime decreases or the particle size increases, and therefore the number of states increases. A larger homogeneity favors the contribution of transitions with large matrix elements, even if they are out of resonance ($\varepsilon_f - \varepsilon_i \ll \hbar\omega$), over transitions satisfying the resonance condition ($\varepsilon_f - \varepsilon_i \approx \hbar\omega$).

Since the total amount of energy dissipated in the carrier generation is fixed by the optical absorption of the nanoparticle, situations in which hot carriers are generated with energies close to the Fermi level must be associated with larger production rates. Similarly, high energy hot carriers are generated in smaller numbers. This is clearly corroborated by the results shown in Figure 3, where we analyze hot carrier production of a D = 15 nm (panel (a)), and a D = 25 nm (panel (b)) silver nanoparticles as a function of the external illumination frequency. We observe that shortening the lifetime or increasing the particle diameter results in a larger number of carriers generated. At the same time, the spectral profile becomes smoother reflecting the increasing homogeneity of the electronic density of states.

Quantifying the Hot Carrier Generation Efficiency. As discussed in the introduction, the plasmon-induced hot carriers can be used in numerous applications. In order to exploit this process, it is important to have a metric that allows for the quantification of the efficiency of different plasmonic systems to generate useful hot carriers. Here we propose a figure of merit (FoM) $\mathcal{N}_e(\varepsilon)$ defined as the number of hot electrons generated per each plasmon excited in the system that have an energy (measured with respect to the Fermi level) larger than a certain threshold ε. This quantity can be written in terms of the generation rate eq 1 and the absorbed power as

$$\mathcal{N}_e(\varepsilon) = \hbar\omega_p \sum_{\varepsilon_f \geq \varepsilon} \Gamma_e(\varepsilon_f, \omega_p)/P_{abs} \qquad (2)$$

Obviously, a similar expression can be defined for the case of hot holes (with energies also measured with respect to the Fermi level), in which $\Gamma_e(\varepsilon_f,\omega_p)$ is substituted by $\Gamma_h(\varepsilon_f,\omega_p)$ and the summation is performed over states with an energy below $-\varepsilon$.

Figure 4 shows the FoM $\mathcal{N}_e(\varepsilon)$ calculated as a function of the particle diameter for four different hot carrier lifetimes. In panel (a) the value of the energy threshold is $\varepsilon = 0.2\hbar\omega_p$, while in panel (b) we chose $\varepsilon = 0.5\hbar\omega_p$. Comparing the two panels we observe that, as expected from its definition, the value of $\mathcal{N}_e(\varepsilon)$ drops as the energy threshold is increased. Furthermore, we note that the efficiency of the carrier generation depends strongly on both the particle size and the carrier lifetime. As a general trend, the efficiency decreases with increasing diameter and increases with increasing lifetime. However, the situation is reversed for the smallest diameter under consideration (D = 5 nm). This anomalous behavior is most likely related to the discreteness of the electronic density of states of this small system, which is not efficiently compensated by the finite carrier lifetime τ.

Directionality and Spatial Distribution of Hot Carriers. The plasmon-induced hot carriers are not distributed uniformly across the nanoparticle volume. On the contrary, their spatial distribution is determined by the electronic wave function of the final state of the transition that generates them. Figure 5(a) shows the hot electron density distribution in a silver nanoparticle

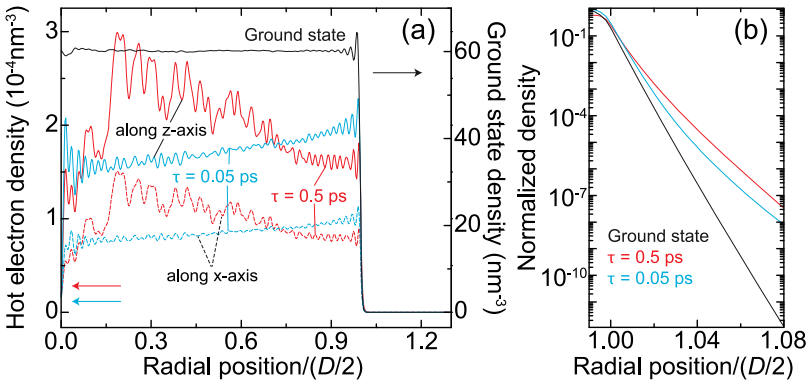

Figure 5. Directionality and spatial distribution of hot carriers. (a) Local density of hot electrons generated in a silver nanoparticle of D = 25 nm at the plasmon frequency (*i.e.*, 3.65 eV) calculated along the axis parallel (solid lines, left scale) and perpendicular (dashed lines, left scale) to the external field polarization. We plot this density for two different hot carrier lifetimes: τ = 0.5 ps (red lines) and τ = 0.05 ps (blue lines). For comparison, we also show the ground state density (black line, right scale). (b) Comparison of the spill-out of the hot electron (red and blue lines) and the ground state (black line) densities along the axis parallel to the external field polarization. In this case the densities are normalized to their maximum value.

with D = 25 nm at the plasmon frequency ($\hbar\omega_p$ = 3.65 eV) for two different carrier lifetimes τ = 0.5 ps (red lines, left scale) and τ = 0.05 ps (blue lines, left scale). The solid lines show the local hot electron density along the axis parallel to the polarization of the external field. The dashed curves show the corresponding quantity in the perpendicular direction and are smaller by approximately a factor of 2. These results show that the hot carriers are primarily generated in the region of the sphere where the field enhancements are large, *i.e.*, along the polarization direction. Interestingly, shorter carrier lifetimes results in more homogeneous spatial distributions, similar to the ground state (black line, right scale), due to the contribution of a larger number of states with smaller energies. Although the hot electrons are confined to the metal nanoparticle, we expect that due to their high energy they will extend further outside the nanoparticle than the ground state electrons. This is clearly shown in Figure 5(b) where we compare the decay of the spatial distribution of the hot electrons outside of the nanoparticle with electron spill-out of the conduction electrons of a nanoparticle in its ground state.

Plasmon-Induced Hot Carriers in Nanoshells. As discussed in previous sections, the spectral profile of the hot carrier generation rate essentially follows the absorption spectrum of the nanoparticle (see Figures 1(b,c)). In the case of small spherical nanoparticles, as the ones considered here, the plasmon resonance is determined exclusively by the material parameters and cannot be tuned. However, in practical applications it is crucial to be able to tune the energies of the hot carriers. A suitable alternative nanoparticle is the metallic nanoshell, whose plasmonic response is highly tunable and can be adjusted by changing the values of the inner and outer diameters.[53] We explore this possibility in Figure 6(a), where the solid blue line (left scale) shows the number of hot electrons generated per unit of time and volume for a nanoshell with inner and outer diameters of 15 and 25 nm, respectively, calculated as a function of the frequency of the external illumination.

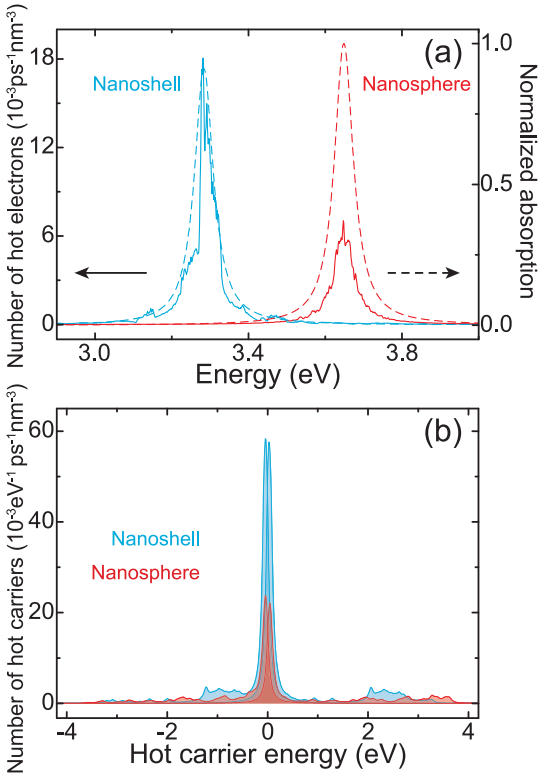

Figure 6. Plasmon-induced hot electrons in nanoshells. (a) Number of hot electrons generated per unit of time and volume as a function of the external illumination frequency for a nanoshell with inner and outer diameters of 15 and 25 nm, respectively (blue solid line, left scale). We compare the results for the nanoshell with those obtained for a nanoparticle of D = 25 nm (red solid line). The absorption associated with these nanostructures is plotted using dashed lines (right scale). (b) Hot carrier spectrum for the nanoshell (blue curve) and the nanoparticle (red curve) of panel (a), calculated at the plasmon frequency ($\hbar\omega_p$ = 3.28 eV for the nanoshell and $\hbar\omega_p$ = 3.65 eV for the nanoparticle). The hot carrier lifetime is fixed to τ = 0.5 ps. Zero energy refers to the Fermi level.

This hot electron generation rate clearly follows the absorption profile (blue dashed line, right scale), and is strongly red-shifted with respect to the case of a solid nanoparticle with D = 25 nm (red lines). The shift, as discussed before, can be adjusted by changing the ratio between the inner and outer diameters. Interestingly, we find that the nanoshell presents a larger generation rate per unit of volume than the solid spherical nanoparticle. This is corroborated by the results shown in panel (b), where we have plotted the carrier energy distribution for these two nanostructures at the plasmon frequency ($\hbar\omega_p$ = 3.28 eV for the nanoshell and $\hbar\omega_p$ = 3.65 eV for the nanoparticle). However, although the nanoshell produces a larger number of carriers, when we calculate its efficiency using the FoM defined in eq 2 we find the values: $\mathcal{N}_e(\varepsilon = 0.2\hbar\omega_p) = 0.84$ and $\mathcal{N}_e(\varepsilon = 0.5\hbar\omega_p) = 0.73$, which are similar to those obtained for the nanoparticle (see Figure 4).

CONCLUSIONS

We have developed a simple model for the description of the plasmon-induced hot carrier generation process in metallic nanoparticles. The model is based on describing the conduction electrons of the metal as free particles in an spherical potential well and then using Fermi's golden rule to calculate hot carrier generation rate induced by the plasmon decay. By substituting the free electron wave functions and energies with those obtained with a DFT methodology we have explicitly shown that many-body effects have only a minor influence on the carrier generation. Using our model we have calculated the number of carriers generated as a function of the frequency of the external illumination and found that this property follows the absorption profile determined by the plasmon resonance. Furthermore, our analysis has revealed that the particle size and the hot carrier lifetime strongly influence the production rate and the energies of the generated hot carriers. In particular, we have found that larger sizes and shorter lifetimes result in higher hot carrier production rates but smaller hot carrier energies, and vice versa. In order to quantify the hot carrier generation efficiency of a certain nanostructure we have introduced a figure of merit defined as the number of hot electrons (or holes) generated per each plasmon excited in the system with an energy larger than a certain threshold. We have also analyzed the spatial distribution of the hot carriers showing that they are predominantly concentrated along the direction parallel to the polarization of the external field, and that they extend further out from the nanoparticle than the unperturbed electron distribution. Additionally, we have studied the hot carrier generation in a nanoshell, which has allowed us to show that by adjusting the size and the thickness of this nanostructure it is possible to tune the energy of the plasmon-induced hot carriers. Our results provide a solid theoretical background for understanding of the plasmon-induced hot carrier generation process and will allow for the design and optimization of novel devices capable of fully exploiting the properties of these excitations.

METHODS

Free Electron Model. Within this approximation the electrons are regarded as free particles moving in a finite spherical potential well. The energy ε and the wave function Ψ of these electrons can be obtained by solving the following Schrödinger equation

$$-\frac{\hbar^2}{2m}\frac{1}{r^2}\frac{\partial}{\partial r}\left(r^2\frac{\partial\Psi}{\partial r}\right)+\frac{L^2}{2mr^2}\Psi+V(r)\Psi = \varepsilon\Psi$$

where L^2 represents the square of the angular momentum operator whose eigenvalues are $\hbar^2 l(l+1)$, m is the electron mass, and $V(r)$, which is equal to V_0 inside the nanoparticle and vanishes outside, defines the potential well. The value V_0 is chosen to obtain the correct workfunction for silver (4.5 eV). Because of the spherical symmetry of the system, the wave functions can be factored into a radial part, $R(r)$, and an angular part given by the spherical harmonics, $Y_l^m(\theta,\phi)$. Upon factorization, we only need to solve the radial Schrödinger equation

$$\left(r^2\frac{d^2}{dr^2}+2r\frac{d}{dr}-2\frac{r^2m}{\hbar^2}[V(r)-\varepsilon]-l(l+1)\right)R(r) = 0. \quad (3)$$

The general solution to eq 3 are the spherical Bessel functions of the first kind $j_l(\alpha r)$ inside the particle boundary and the spherical Hankel functions of the first kind $h_l(i\kappa r)$ outside the particle boundary with $\alpha = (-2m/\hbar^2(V(r)-\varepsilon))^{1/2}$ and $\kappa = (-2m/\hbar^2\varepsilon)^{1/2}$. By imposing continuity and differentiability at the surface, the full spectrum of wave functions and energies is found.

DFT Formalism. The free electron model, as its own name indicates, neglects any interaction between the electrons. Therefore, in order to incorporate many-body effects for the conduction electrons we employ Kohn–Sham orbitals taken from density functional theory (DFT) calculations. In particular, we follow a methodology previously described[54] in which the ground state wave functions and energies are found by solving eq 3 with $V(r) = V_{eff}(r)$, which now includes a background pseudopotential V_0, the Hartree potential, and the exchange correlation potential V_{xc}

$$V_{eff}(r) = V_0(r)+\int\frac{n(r')-n_0(r')}{|\mathbf{r}-\mathbf{r}'|}d\mathbf{r}'+V_{xc}[n(r)]$$

Here, $n(r)$ is the electron density and $n_0(r)$ is the positive pseudoionic density associated with the jellium model. Again, V_0 is adjusted to recover the correct workfunction of silver, 4.5 eV.

Conflict of Interest: The authors declare no competing financial interest.

Acknowledgment. This work has been supported in part by the Robert A. Welch Foundation under Grant C-1222, and the Shared University Grid At Rice (SUGAR) funded by NSF under Grant E1A-0216467, and a partnership between Rice University, Sun Microsystems and Sigma Solutions, Inc. A. M. acknowledges financial support from the Welch foundation through the J. Evans Attwell-Welch Postdoctoral Fellowship Program of the Smalley Institute of Rice University (Grant No. L-C-004).

REFERENCES AND NOTES

1. Novotny, L.; Hecht, B. *Principles of Nano-Optics*; Cambridge University Press: New York, 2006.
2. Maier, S. A. *Plasmonics: Fundamentals and Applications*; Springer: New York, 2007.

3. Halas, N. J.; Lal, S.; Chang, W.; Link, S.; Nordlander, P. Plasmons in Strongly Coupled Metallic Nanostructures. *Chem. Rev.* **2011**, *111*, 3913–3961.
4. Xu, H.; Bjerneld, E. J.; Käll, M.; Börjesson, L. Spectroscopy of Single Hemoglobin Molecules by Surface Enhanced Raman Scattering. *Phys. Rev. Lett.* **1999**, *83*, 4357–4360.
5. Álvarez-Puebla, R. A.; Liz-Marzán, L. M.; García de Abajo, F. J. Light Concentration at the Nanometer Scale. *J. Phys. Chem. Lett.* **2010**, *1*, 2428–2434.
6. O'Neal, D. P.; Hirsch, L. R.; Halas, N. J.; Payne, J. D.; West, J. L. Photo-Thermal Tumor Ablation in Mice Using Near Infrared-Absorbing Nanoparticles. *Cancer Lett.* **2004**, *209*, 171–176.
7. Loo, C.; Lowery, A.; Halas, N. J.; West, J. L.; Drezek, R. Inmunotargeted Nanoshells for Integrated Cancer Imaging and Therapy. *Nano Lett.* **2005**, *5*, 709–711.
8. Luo, Y. L.; Shiao, Y. S.; Huang, Y. F. Release of Photoactivatable Drugs from Plasmonic Nanoparticles for Targeted Cancer Therapy. *ACS Nano* **2011**, *5*, 7796–7804.
9. Huschka, R.; Zuloaga, J.; Knight, M. W.; Brown, L. V.; Nordlander, P.; Halas, N. J. Light-Induced Release of DNA from Gold Nanoparticles: Nanoshells and Nanorods. *J. Am. Chem. Soc.* **2011**, *133*, 12247–12255.
10. Atwater, H. A.; Polman, A. Plasmonics for Improved Photovoltaic Devices. *Nat. Mater.* **2010**, *9*, 205–213.
11. Salvador, M.; MacLeod, B. A.; Hess, A.; Kulkarni, A. P.; Munechika, K.; Chen, J. I. L.; Ginger, D. S. Electron Accumulation on Metal Nanoparticles in Plasmon-Enhanced Organic Solar Cells. *ACS Nano* **2012**, *6*, 10024–10032.
12. Curto, A. G.; Volpe, G.; Taminiau, T. H.; Kreuzer, M. P.; Quidant, R.; van Hulst, N. F. Unidirectional Emission of a Quantum Dot Coupled to a Nanoantenna. *Science* **2010**, *329*, 930–933.
13. Giannini, V.; Fernández-Domínguez, A. I.; Heck, S. C.; Maier, S. A. Plasmonic Nanoantennas: Fundamentals and Their Use in Controlling the Radiative Properties of Nanoemitters. *Chem. Rev.* **2011**, *111*, 3888–3912.
14. Novotny, L.; Van Hulst, N. Antennas for Light. *Nat. Photonics* **2011**, *5*, 83–90.
15. Wu, K.; RodrÂguez-Córdoba, W. E.; Yang, Y.; Lian, T. Plasmon-Induced Hot Electron Transfer from the Au Tip to CdS Rod in CdS-Au Nanoheterostructures. *Nano Lett.* **2013**, *13*, 5255–5263.
16. Clavero, C. Plasmon-Induced Hot-Electron Generation at Nanoparticle/Metal-Oxide Interfaces for Photovoltaic and Photocatalytic Devices. *Nat. Photonics* **2014**, *8*, 95–103.
17. Wu, X.; Thrall, E. S.; Liu, H.; Steigerwald, M.; Brus, L. Plasmon Induced Photovoltage and Charge Separation in Citrate-Stabilized Gold Nanoparticles. *J. Phys. Chem. C* **2010**, *114*, 12896–12899.
18. Ingram, D. B.; Linic, S. Water Splitting on Composite Plasmonic-Metal/Semiconductor Photoelectrodes: Evidence for Selective Plasmon-Induced Formation of Charge Carriers near the Semiconductor Surface. *J. Am. Chem. Soc.* **2011**, *133*, 5202–5205.
19. Gomes Silva, C.; Juárez, R.; Marino, T.; Molinari, R.; GarcíÂa, H. Influence of Excitation Wavelength (UV or Visible Light) on the Photocatalytic Activity of Titania Containing Gold Nanoparticles for the Generation of Hydrogen or Oxygen from Water. *J. Am. Chem. Soc.* **2011**, *133*, 595–602.
20. Lee, J.; Mubeen, S.; Ji, X.; Stucky, G. D.; Moskovits, M. Plasmonic Photoanodes for Solar Water Splitting with Visible Light. *Nano Lett.* **2012**, *12*, 5014–5019.
21. Thomann, I.; Pinaud, B. A.; Chen, Z.; Clemens, B. M.; Jaramillo, T. F.; Brongersma, M. L. Plasmon Enhanced Solar-to-Fuel Energy Conversion. *Nano Lett.* **2011**, *11*, 3440–3446.
22. Chen, H. M.; Chen, C. K.; Chen, C.-J.; Cheng, L.-C.; Wu, P. C.; Cheng, B. H.; Ho, Y. Z.; Tseng, M. L.; Hsu, Y.-Y.; Chan, T.-S.; *et al.* Plasmon Inducing Effects for Enhanced Photoelectrochemical Water Splitting: X-ray Absorption Approach to Electronic Structures. *ACS Nano* **2012**, *6*, 7362–7372.
23. Mubeen, S.; Lee, J.; Singh, N.; Kramer, S.; Stucky, G. D.; Moskovits, M. An Autonomous Photosynthetic Device in Which All Charge Carriers Derive from Surface Plasmons. *Nat. Nanotechnol.* **2013**, *8*, 247–251.
24. Mukherjee, S.; Libisch, F.; Large, N.; Neumann, O.; Brown, L. V.; Cheng, J.; Lassiter, J. B.; Carter, E. A.; Nordlander, P.; Halas, N. J. Hot Electrons Do the Impossible: Plasmon-Induced Dissociation of H2 on Au. *Nano Lett.* **2013**, *13*, 240–247.
25. Mukherjee, S.; Zhou, L.; Goodman, A. M.; Large, N.; Ayala-Orozco, C.; Zhang, Y.; Nordlander, P.; Halas, N. J. Hot-Electron-Induced Dissociation of H2 on Gold Nanoparticles Supported on SiO_2. *J. Am. Chem. Soc.* **2014**, *136*, 64–67.
26. Murdoch, M.; Waterhouse, G. I. N.; Nadeem, M. A.; Metson, J. B.; Keane, M. A.; Howe, R. F.; Llorca, J.; Idriss, H. The Effect of Gold Loading and Particle Size on Photocatalytic Hydrogen Production from Ethanol over Au/TiO2 Nanoparticles. *Nat. Chem.* **2011**, *3*, 489–492.
27. Seh, Z. W.; Liu, S.; Low, M.; Zhang, S.-Y.; Liu, Z.; Mlayah, A.; Han, M.-Y. Janus Au-TiO2 Photocatalysts with Strong Localization of Plasmonic Near-Fields for Efficient Visible-Light Hydrogen Generation. *Adv. Mater.* **2012**, *24*, 2310–2314.
28. Linic, S.; Christopher, P.; Ingram, D. B. Plasmonic-Metal Nanostructures for Efficient Conversion of Solar to Chemical Energy. *Nat. Mater.* **2011**, *10*, 911–921.
29. Baffou, G.; Quidant, R. Nanoplasmonics for Chemistry. *Chem. Soc. Rev.* **2014**, *43*, 3898–3907.
30. Lee, Y. K.; Jung, C. H.; Park, J.; Seo, H.; Somorjai, G. A.; Park, J. Y. Surface Plasmon-Driven Hot Electron Flow Probed with Metal-Semiconductor Nanodiodes. *Nano Lett.* **2011**, *11*, 4251–4255.
31. García de Arquer, F. P.; Mihi, A.; Kufer, D.; Konstantatos, G. Photoelectric Energy Conversion of Plasmon-Generated Hot Carriers in Metal-Insulator-Semiconductor Structures. *ACS Nano* **2013**, *7*, 3581–3588.
32. Conklin, D.; Nanayakkara, S.; Park, T.-H.; Lagadec, M. F.; Stecher, J. T.; Chen, X.; Therien, M. J.; Bonnell, D. A. Exploiting Plasmon-Induced Hot Electrons in Molecular Electronic Devices. *ACS Nano* **2013**, *7*, 4479–4486.
33. Schwede, J. W.; Bargatin, I.; Riley, D. C.; Hardin, B. E.; Rosenthal, S. J.; Sun, Y.; Schmitt, F.; Pianetta, P.; Howe, R. T.; Shen, Z.-X.; *et al.* Photon-Enhanced Thermionic Emission for Solar Concentrator Systems. *Nat. Mater.* **2011**, *9*, 762–767.
34. Atar, F. B.; Battal, E.; Aygun, L. E.; Daglar, B.; Bayindir, M.; Okyay, A. K. Plasmonically Enhanced Hot Electron Based Photovoltaic Device. *Opt. Express* **2013**, *21*, 7196–7201.
35. Goykhman, I.; Desiatov, B.; Khurgin, J.; Shappir, J.; Levy, U. Locally Oxidized Silicon Surface-Plasmon Schottky Detector for Telecom Regime. *Nano Lett.* **2011**, *11*, 2219–2224.
36. Knight, M. W.; Sobhani, H.; Nordlander, P.; Halas, N. J. Photodetection with Active Optical Antennas. *Science* **2011**, *332*, 702–704.
37. Chalabi, H.; Schoen, D.; Brongersma, M. L. Hot-Electron Photodetection with a Plasmonic Nanostripe Antenna. *Nano Lett.* **2014**, *14*, 1374–1380.
38. Fang, Z.; Wang, Y.; Liu, Z.; Schlather, A.; Ajayan, P. M.; Koppens, F. H. L.; Nordlander, P.; Halas, N. J. Plasmon-Induced Doping of Graphene. *ACS Nano* **2012**, *6*, 10222–10228.
39. Hoggard, A.; Wang, L.-Y.; Ma, L.; Fang, Y.; You, G.; Olson, J.; Liu, Z.; Chang, W.-S.; Ajayan, P. M.; Link, S. Using the Plasmon Linewidth To Calculate the Time and Efficiency of Electron Transfer between Gold Nanorods and Graphene. *ACS Nano* **2013**, *7*, 11209–11217.
40. Appavoo, K.; Wang, B.; Brady, N. F.; Seo, M.; Nag, J.; Prasankumar, R. P.; Hilton, D. J.; Pantelides, S. T.; Haglund, R. F. Ultrafast Phase Transition *via* Catastrophic Phonon Collapse Driven by Plasmonic Hot-Electron Injection. *Nano Lett.* **2014**, *14*, 1127–1133.
41. Frischkorn, C.; Wolf, M. Femtochemistry at Metal Surfaces: Nonadiabatic Reaction Dynamics. *Chem. Rev.* **2006**, *106*, 4207–4233.
42. White, T. P.; Catchpole, K. R. Plasmon-Enhanced Internal Photoemission for Photovoltaics: Theoretical Efficiency Limits. *Appl. Phys. Lett.* **2012**, *101*, 073905.
43. Kornbluth, M.; Nitzan, A.; Seideman, T. Light-Induced Electronic Non-Equilibrium in Plasmonic Particles. *J. Chem. Phys.* **2013**, *138*, 174707.

44. Govorov, A. O.; Zhang, H.; Gun'ko, Y. K. Theory of Photoinjection of Hot Plasmonic Carriers from Metal Nanostructures into Semiconductors and Surface Molecules. *J. Phys. Chem. C* **2013**, *117*, 16616–16631.
45. Zhang, H.; Govorov, A. O. Optical Generation of Hot Plasmonic Carriers in Metal Nanocrystals: The Effects of Shape and Field Enhancement. *J. Phys. Chem. C* **2014**, *118*, 7606–7614.
46. Govorov, A. O.; Zhang, H.; Demir, H. V.; Gun'ko, Y. K. Photogeneration of Hot Plasmonic Electrons with Metal Nanocrystals: Quantum Description and Potential Applications. *Nano Today* **2014**, *9*, 85–101.
47. Ashcroft, N. W.; Mermin, N. D. *Solid State Physics*; Harcourt College Publishers: New York, 1976.
48. Messiah, A. *Quantum Mechanics*; North-Holland: New York, 1966.
49. Link, S.; El-Sayed, M. A. Spectral Properties and Relaxation Dynamics of Surface Plasmon Electronic Oscillations in Gold and Silver Nanodots and Nanorods. *J. Phys. Chem. B* **1999**, *103*, 8410–8426.
50. Bigot, J.-Y.; Halté, V.; Merle, J.-C.; Daunois, A. Electron Dynamics in Metallic Nanoparticles. *Chem. Phys.* **2000**, *251*, 181–203.
51. Voisin, C.; Del Fatti, N.; Christofilos, D.; Vallée, F. Ultrafast Electron Dynamics and Optical Nonlinearities in Metal Nanoparticles. *J. Phys. Chem. B* **2001**, *105*, 2264–2280.
52. Du, L.; Furube, A.; Hara, K.; Katoh, R.; Tachiya, M. Ultrafast Plasmon Induced Electron Injection Mechanism in Gold-TiO_2 Nanoparticle System. *J. Photochem. Photobiol., C* **2013**, *15*, 21–30.
53. Oldenburg, S.; Averitt, R.; Westcott, S.; Halas, N. Nanoengineering of Optical Resonances. *Chem. Phys. Lett.* **1998**, *288*, 243–247.
54. Prodan, E.; Nordlander, P. Electronic Structure and Polarizability of Metallic Nanoshells. *Chem. Phys. Lett.* **2002**, *352*, 140–146.